Acta Geochim (2025) 44:1293–1307
https://doi.org/10.1007/s11631-025-00786-7

ORIGINAL ARTICLE

Triassic diorites in the Qinling orogen: Underappreciated role for gold metallogeny in continental collision orogenic belt

Hua Zhang[1] · Kai Zhang[2] · Xi Zhu[2] · Jiangfeng Qin[1] · Shaohua Mao[2] · Lisha Bi[2]

Received: 4 December 2024 / Revised: 4 April 2025 / Accepted: 12 May 2025 / Published online: 10 July 2025
© The Author(s), under exclusive licence to Science Press and Institute of Geochemistry, CAS and Springer-Verlag GmbH Germany, part of Springer Nature 2025

Abstract The Triassic granitoids and associated diorites in the Qinling orogenic belt reveal critical evidence of crust–mantle interaction during the terminal collision between the North China and Yangtze Blocks. This study presents new constraints from zircon U–Pb age, Lu–Hf isotopes, and amphibole-plagioclase-apatite geochemistry for the Maoerliang diorite in the Foping area. Zircon U–Pb dating yields a crystallization age of 212 ± 2.8 Ma, with εHf(t) values ranging from −8.6 to +3.0 and corresponding two-stage Hf model ages (T_{DM2}) of 886–1479 Ma, indicative of derivation from an evolved lithospheric mantle source. Petrogenetic indicators reveal a mantle affinity: amphiboles exhibit high MgO (9.8–11.2 wt%) and elevated Nb/Ta ratios (14.3–18.1), while apatites display F-rich (2.1–2.8 wt%) and Cl-poor (0.08–0.15 wt%) characteristics. Thermobarometric calculations based on amphibole chemistry constrain crystallization conditions of 805–866 °C and 211–383 MPa, corresponding to mid-crustal emplacement depths (8–14 km). Both amphibole and zircon indicate elevated oxygen fugacity (ΔNNO = −4.08 to −3.71; ΔFMQ = −1.14 to +3.96) and hydrous magma conditions (H_2O = 4.22–4.94 wt%). Late-stage plagioclase crystallization (An21–26.5) reflects prolonged fractional crystallization in a hydrous dioritic magma. These diagnostic features—mantle-derived signatures, high fO_2, and hydrous nature—exhibit remarkable convergence with gold-mineralized granites in the East Qinling. Our findings suggest that Triassic dioritic magmatism may have played an underappreciated role in facilitating gold enrichment processes within the South Qinling metallogenic belt.

Keywords South Qinling · Hydrous diorite · Heterogeneous source · Amphibole · Apatite chemistry

1 Introduction

Appinite represents amphibole-rich diorire, which is closely associated with high-Ba–Sr granites in collisional orogenic belts, providing significant insight into the properties of the metasomatized mantle lithosphere (Murphy 2020; Iveson et al. 2021; Chang et al. 2021). Appinite also preserves information about metasomatic agents of the lithospheric mantle (Zhang et al. 2012; Murphy 2013, 2020; Laurent et al. 2017; Pe-Piper et al. 2018). Moreover, the residual fluids in the late crystallization stage of appinite are pivotal for the high degree of crustal melting and the genesis of granites (Collins et al. 2020). Globally, typical appinites are commonly associated with high-Ba–Sr granites (Tarney and

Supplementary Information The online version contains supplementary material available at https://doi.org/10.1007/s11631-025-00786-7.

✉ Jiangfeng Qin
qinjf@nwu.edu.cn

Hua Zhang
3213953544@qq.com

Kai Zhang
zhangkai1663@163.com

Xi Zhu
zhuxi_nwu@foxmail.com

Shaohua Mao
540147176@qq.com

Lisha Bi
1716351893@qq.com

[1] Department of Geology, Northwest University/State Key Laboratory of Continental Dynamics, Xi'an 710069, Shaanxi Province, China

[2] Shaanxi Geological Science and Technology Center, Xi'an 710054, Shaanxi Province, China

Jones 1994; Zhang et al. 2012; Zhong et al. 2016; Yuan et al. 2016; Murphy 2020 Leite et al. 2021). Prominent examples include the Late Silurian Aping Complex in Scotland and the Early Carboniferous Diorite in Spain (Castro et al. 2003; Murphy 2013). Notably, the Late Archean appinites in the Subilier are posited to be associated with the initiation of the Late Archean plate tectonics (Stern et al. 1989).

The Qinling-Dabie orogenic belt was the product of the Triassic collision between the North China and Yangtze Blocks, which resulted in voluminous granitic rocks and associated Mo-W mineralization events in the Qinling orogenic belt (Qin et al. 2010, 2013, 2019; Dong et al. 2021), including granodiorite, contemporaneous mafic enclaves (Wang et al. 2011a, b; Zhang et al. 2008; Qin et al. 2010), and some amphibole-rich diorite. Systematic zircon U–Pb dating indicates that the Triassic granites in the south Qinling were concentrated between 248 and 190 Ma (Liu et al. 2011; Qin et al. 2010, 2013; Yang et al. 2011, 2013). Qin et al. (2013) integrated geological, petrological, geochemical, and isotopic data to divide these granites into three periods: (1) 235–220 Ma, granodiorite, tonalite, and monzogranite formed during the subduction period; (2) 215–201 Ma, monzogranite formed during the transition from syn-collision to post-collision; and (3) 200–190 Ma, granites with S-type affinity formed in the post-collision setting. Geochemical and isotopic studies suggest that these granites originated from the melting of the Neoproterozoic basaltic lower crust, and the contemporaneous mafic enclaves represent mantle-derived magma, which played a significant role in the crustal melting events (Qin et al. 2013). However, the Triassic crust–mantle interaction mechanisms in the Qinling orogenic belt are still debated, especially the source region of the amphibole-rich diorite.

This paper selects the diorite from the Maoerliang, southern Foping, for zircon U–Pb dating, Lu–Hf isotope, and mineral chemistry, aiming to reveal the source region and crystallization conditions. The results indicate that these diorites represent hydrous appinite that originating from a metasomatized mantle lithosphere.

2 Geological background and field geology

The Qinling orogenic belt is bounded by the Lingbao-Lushan-Wuyang fault (LLWF) to the north and the Mianlue-Bashan-Xiangguang fault (MBXF) to the south (Fig. 1a) (Dong et al. 2016). From north to south, it is sequentially composed of the Kuanping, Shangdan, and Mianlue tectonic zones (Zhang et al. 2001; Dong et al. 2011, 2014). Based on the three fault zones, the Qinling orogenic belt can be further divided into four tectonic units, namely the southern margin of the North China Block, the North Qinling (NQB), the South Qinling (SQB), and the northern margin of the Yangtze Block (Fig. 1a) (Dong et al. 2013, 2014). The South Qinling (SQB) is located between the Shangdan suture zone and the Mianlue suture zone, and is composed of Precambrian crystalline basement, overlain by Paleozoic sediment, and intruded by Mesozoic granites (Wang et al. 2011a, b, 2015; Dong et al. 2011; Yang et al. 2013). The Precambrian crystalline basement includes the Archean Yudongzi Group and the Proterozoic Foping, Douling, Yaolinghe and Wudang Group (Zhang et al. 2001; Shi et al. 2013). The Yudongzi Group (2703–2527 Ma) is composed of granitic gneiss, amphibolite, green schist, quartzite, and the Neoarchean trondhjemite-tonalite-granodiorite (TTG) suite (Wang et al. 2011a, b; Qin et al. 1992; Wu et al. 2014; Zhang et al. 2010). The Triassic granites (Fig. 1b) include the Guangtoushan pluton in the western segment, the Huayang-Wulong pluton in the central segment, and the Dongjiangkou-Shahewan pluton (Dong et al. 2011; Yang et al. 2013; Chen et al. 2009; Deng et al. 2016; Liu et al. 2011). Zircon U–Pb dating indicate that these granites were formed between 248–190 Ma (Yang et al. 2011, 2014, 2013; Wang et al. 2011a, b; Qin et al. 2010, 2013; Dong et al. 2011, 2012; Liu et al. 2011; Hu et al. 2016), and there are systematic differences in geochemical properties, source region, and metallogenic specificity in different stages, reflecting the variations in crustal levels during different stages of the collision process.

The Maoerliang diorite is located in the southern part of Foping County, which is part of the Triassic Wulong pluton, covering an area of 24 km^2. It mainly intrudes the Proterozoic Foping Group (Fig. 1b). The diorite exhibits a medium-coarse-grained texture (Fig. 2), with the main minerals including plagioclase (40%–45%), amphibole (40%–45%), K-feldspar (< 5%), quartz (< 10%), and biotite (5%–10%). Plagioclase occurs as coarse, hypautomorphic tabular crystals, about 3–6 mm in size, with Carlsbad-albite twinning. Amphibole displays a euhedral prismatic shape and occurs as mafic clusters, with similar grain size of 3–6 mm, and some amphibole has a clinopyroxene core (Fig. 2a). Quartz has smaller grain size of 0.5–1 mm; biotite is brown, mainly distributed in the interstices of feldspar grains. Accessory minerals include zircon, apatite, allanite, epidote, and magnetite. Apatite occurs as rod-like or prismatic crystals, mainly as inclusions within biotite, amphibole, and plagioclase, while zircon typically occurs as prismatic, euhedral crystals.

3 Analytical method

3.1 Zircon U–Pb and Lu–Hf isotopes

Zircon grains were separated using traditional heavy liquid and magnetic separation techniques. Representative zircon grains were handpicked, mounted in epoxy resin

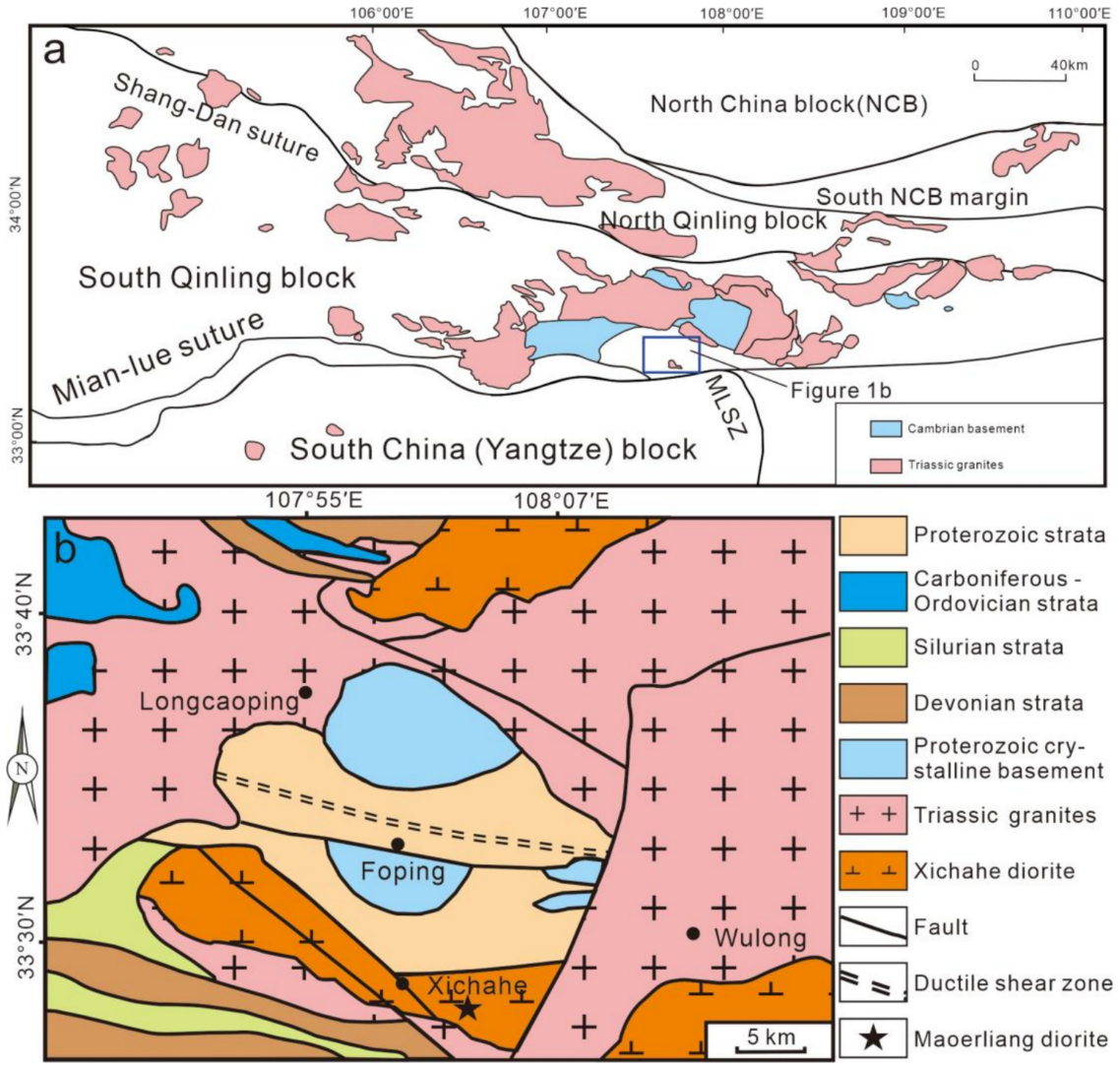

Fig. 1 **a** Geological sketch map of the Qinling orogenic belt, showing the distribution of Indosinian granites. **b** Geological sketch map of the Foping area in the South Qinling Mountains (modified from Qin et al. 2007)

disks, and then polished and carbon-coated. Before conducting U–Pb and Lu–Hf isotope analyses, these grains were inspected using cathodoluminescence (CL) imaging. Zircon U–Pb analysis by laser ablation inductively coupled plasma mass spectrometry (ICP-MS) was performed following the method described by Yuan et al. (2008) on an Agilent 7500a ICP-MS equipped with a 193 nm laser. The weighted average $^{206}Pb/^{238}U$ ages for the standard zircon 91500 and GJ-1 were 1064.2 ± 3.1 Ma ($n = 14$, 2σ) and 603.1 ± 3.4 Ma ($n = 12$, 2σ), respectively, which are in good agreement with the recommended isotope dilution thermal ionization mass spectrometry (ID-TIMS) ages (Wiedenbeck et al. 1995). Detailed analytical methods can be found in Yuan et al. (2008). The determination of common lead followed the method by Anderson et al. (1995). Plotting and age calculations were completed using ISOPLOT v.3.0 (Ludwig 2003).

In situ analysis of zircon Hf isotopes was performed on a high-precision isotope ratio multi-collector neutronium (Nu) plasma mass spectrometer with a 193 nm laser ablation sampling system. During the analysis, the laser spot size was 44 μm, with a repetition rate of 10 Hz and energy of 100 mJ. The $^{176}Yb/^{172}Yb$ value of 0.5887 and the average βYb value obtained from Hf analysis at the same point were used for the interference correction of $^{176}Yb/^{176}Hf$. Detailed analytical methods can be found in Yuan et al. (2008). In the analysis, the standard zircon (91500) had $^{176}Hf/^{177}Hf$ and $^{176}Lu/^{177}Hf$ ratios of 0.282294 ± 15 (2σ, $n = 20$) and 0.00031, respectively, which are similar to the solution-method-measured $^{176}Hf/^{177}Hf$ ratios of 0.282302 ± 8 and 0.282306 ± 8 (2σ). The definitions of εHf(t), $f_{Lu/Hf}$, T_{DM1}

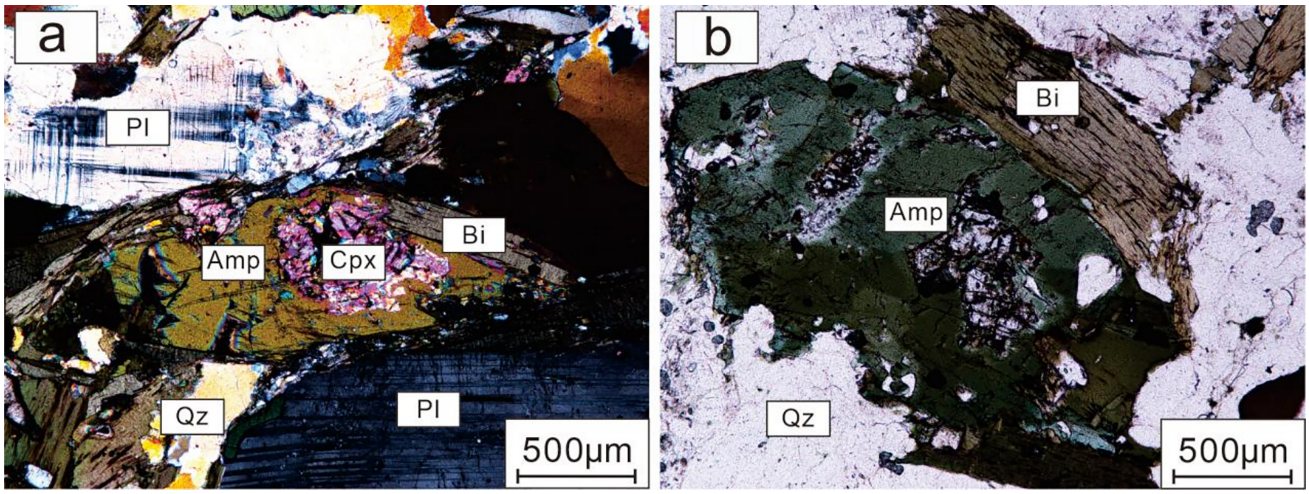

Fig. 2 Microscope photographs of the Maoerliang diorite. Pl. plagioclase; Amp. amphibole; Cpx. clinopyroxene; Bi. biotite; Qz. quartz

(one-stage model age), and T_{DM2} (two-stage model age) are given in Yuan et al. (2008).

3.2 Major elements of minerals (EPMA)

The major element composition was determined using electron probe microanalysis (EPMA) (JEOL JXA-8230 electron probe microanalyzer). The accelerating voltage was set at 15 kV, with a beam current of 10 nA and a beam diameter of 1 μm. Natural and synthetic microprobe standards provided by Spitznagel (SPI) were used, including jade for Si, Al, and Na; diopside for Ca; olivine for Mg; orthoclase for K; hematite for Fe; rhodochrosite for Mn; and rutile for Ti. The analytical errors for these major elements are generally less than 2%.

3.3 Trace elements of minerals (LA-ICP-MS)

Trace element analysis was conducted at the State Key Laboratory of Continental Dynamics, Northwest University using an Agilent 7900 ICP-MS (Agilent Technologies, USA), coupled with a RESOlution S-155 193 nm ArF excimer laser ablation (LA) system (Resonetics, Australia). The ICP-MS is a single-collector mass spectrometer that collects data in peak-hopping mode, acquiring data for one point per mass peak. The integration time for all elements was 15 ms. The high-frequency generator power radio frequency (RF) was set at 1350 W. The carrier gas flowing through the ablation cell was He gas at a flow rate of 280 mL/min, mixed with the working gas Ar gas (flow rate of 1.16 L/min) connected after the ablation cell. Laser ablation was performed using single-point ablation, with a set of NIST 610, NIST 612, BCR-2G, and BHVO-2G standards inserted after every ten sample points for multi-external standard–single internal standard calibration, using Si as the internal standard element. The total test time for each analytical point was 115 s, including 20 s for initial background signal collection, 45 s for laser ablation sample signal collection, and 50 s for flushing the sample introduction system without carrying samples. The ablation spot beam was 67 μm, with an ablation frequency of 6 Hz. Data processing was completed using the ICP-MS DataCal software (Liu et al. 2008). For specific analytical test procedures, refer to Bao et al. (2016).

4 Results

4.1 Zircon U–Pb Age and trace elements

The CL images of the Maoerliang diorite show (Fig. 3) that the zircon grains are euhedral and dark gray in color, with grain sizes ranging from 200 to 300 μm, and most grains exhibit well-developed oscillatory zoning. The results of the zircon U–Pb geochronology analysis are presented in Table 1. Among the 20 zircon grains measured, the U content ranges from 193 to 377 ppm, and the Th content ranges from 94 to 292 ppm, with a Th/U ratio of 0.4 to 0.8, indicating magmatic zircons. The $^{206}Pb/^{238}U$ ages of the diorite range from 203 ± 3 Ma to 221 ± 3 Ma, with a weighted average age of 212 ± 2.8 Ma (n = 20; MSWD = 0.92) (Fig. 4), suggesting that the crystallization age of the Maoerliang diorite was the Late Triassic.

The zircon has Ti content ranging from 2.12 to 18.95 ppm, Ce content ranging from 2.1 to 136 ppm, and total rare earth element (ΣREE) content ranging from 300 to 851 ppm, with an average of 479 ppm. The zircon displays a chondrite-normalized pattern characterized by light rare earth element (LREE) depletion and heavy rare earth element (HREE)

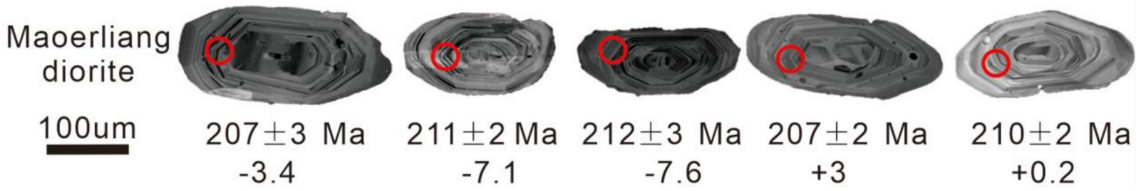

Fig. 3 Cathodoluminescence (CL) images of representative zircons in the Maoerliang diorite. Red circles denote the analytical spots, together with zircon U–Pb ages (Ma) and $\varepsilon_{Hf}(t)$ values

enrichment (Fig. 5), with $(Yb/Gd)_N$ ratios ranging from 5.48 to 10.9 and $(Sm/La)_N$ ratios from 0.01 to 0.1. It has an obvious positive Ce anomaly, with Ce/Ce* ratios ranging from 1.24 to 28.9, and a significant negative Eu anomaly, with Eu/Eu* ratios from 0.24 to 0.46 (Table 2).

4.2 Zircon Lu–Hf isotope

The data analysis results for the zircon Hf isotopes are presented in Table S3. The $^{176}Lu/^{177}Hf$ ratios of the zircon samples range from 0.00032 to 0.00094, which are significantly lower than 0.002, indicating that radiogenic Hf from decay is minimal (Wu et al. 2007). The $f_{Lu/Hf}$ ratios of the zircons (with an average of 0.98) are markedly lower than that of the continental crust; thus, the two-stage model ages more accurately reflect the characteristics of their source regions (Wu et al. 2007). In the diorite, the $\varepsilon_{Hf}(t)$ values of the zircons are primarily negative (−8.6 to −3.0), with two-stage model ages ranging from 1199 to 1479 Ma; only two zircons have positive $\varepsilon_{Hf}(t)$ values (+2.3 and +3.0), with two-stage model ages of 886 to 924 Ma, suggesting that they originate from a mixed crust–mantle source region (Fig. 6). The $\varepsilon_{Hf}(t)$ values of the Maoerliang diorite are relatively consistent with those of the neighboring granites, mainly negative with a few positive values, indicating that the magma in this area may have originated from the same source region (Lu et al. 2016; Wang et al. 2021; Wang et al. 2022).

4.3 Mineral chemistry

4.3.1 Amphibole

The results of the electron microprobe analysis of amphibole in the Maoerliang diorite are presented in Table S4. Amphibole is euhedral to hypautomorphic, some amphibole grains having clinopyroxene cores. The amphibole in the Maoerliang diorite is magnesiohornblende (Leake et al. 1997) (Fig. 7a), with consistent chemical composition, SiO_2 = 43.3–48.6 wt.%, Al_2O_3 = 6.42–10.9 wt.%, TiO_2 = 0.50–1.56 wt.%, FeO^T = 14.0–16.4 wt.%, MnO = 0.31–0.48 wt.%, MgO = 9.9–12.9 wt.%, with high Mg# values of 55.8–66.0, CaO = 11.1–12.4 wt.%, Na_2O = 0.82–1.68 wt.%, and K_2O = 0.58–1.29 wt.%. Amphibole has total rare earth element (∑REE) content of 130 to 184 ppm (Table S5) with "M" shape patterns, slightly enriched in MREE, and negative Eu anomalies (Fig. 8a), which are related to the crystallization of plagioclase. It is enriched in Pb, Rb, and Nd, and depleted in Sr, U, and Th (Fig. 8b). The Nb/Ta ratio ranges from 14.6 to 46.9, and the Zr/Hf ratio ranges from 14.8 to 22.1.

4.3.2 Plagioclase

The electron microprobe results for plagioclase are presented in Table S6. Feldspar in the Maoerliang diorite includes plagioclase and alkali feldspar. The plagioclase is primarily oligoclase with a twin structure, with An values ranging from 21 to 26.5 (Fig. 7b).

4.3.3 Apatite

The major element test results for apatite are presented in Table S7. The apatites in the diorite have CaO=53.5–55.5 wt.%, P_2O_5=40.7–43.9 wt.%, and high F content and F/Cl ratios (77–690) (Fig. 9), with F=2.67–4.00 wt.%, SiO_2=0.04–0.35 wt.%, and SO_3=0.04–0.19 wt.%.

5 Discussion

5.1 Crust–mantle mixing source region for the Maoerliang diorite

The Maoerliang diorite displays identical zircon U–Pb ages and geochemical features to other Late-Triassic granodiorite (Qin et al. 2010, 2013, 2019; Deng et al. 2016; He et al. 2023; Zhang et al. 2019) in the Qinling Orogenic Belt. Previous studies (Qin et al. 2007) indicate that these Late-Triassic intermediate igneous rocks have high MgO and Cr content, with high Mg# values and Sr/Y, La/Yb and Nb/Ta ratios, suggesting that they originated from a crust–mantle mixing source region. Amphiboles in the Maoerliang diorite are mainly magnesiohornblende, as shown in the Al_2O_3–TiO_2 and Ca–Mg–$(Fe^{2+}+Fe^{3+})$ discrimination diagram. For all the amphibole plotted in the field of the crust–mantle mixing zone (Fig. 10), their high Nb/Ta ratios (14.6 to 46.9) are

Table 1 Results of zircon LA-ICP-MS U–Pb analysis for the Maoerliang diorite

Analysis	Content (ppm)				Ratios			
	Th	U	t[(a)]	Th/U	$^{207}Pb/^{206}Pb$	2σ	$^{207}Pb/^{235}U$	2σ
ML-Zr-03	116	213	662	0.54	0.049	0.002	0.226	0.01
ML-Zr-04	107	215	689	0.5	0.057	0.004	0.252	0.017
ML-Zr-05	94	194	706	0.48	0.055	0.003	0.245	0.011
ML-Zr-06	101	205	688	0.49	0.052	0.002	0.244	0.01
ML-Zr-09	124	240	736	0.52	0.055	0.002	0.251	0.01
ML-Zr-11	195	276	666	0.71	0.05	0.002	0.24	0.009
ML-Zr-12	134	227	687	0.59	0.051	0.003	0.245	0.012
ML-Zr-13	145	249	672	0.58	0.055	0.004	0.242	0.019
ML-Zr-17	142	278	689	0.51	0.049	0.002	0.229	0.011
ML-Zr-18	99	193	724	0.51	0.052	0.003	0.241	0.015
ML-Zr-19	163	277	712	0.59	0.056	0.003	0.265	0.015
ML-Zr-21	97	241	680	0.4	0.053	0.004	0.24	0.019
ML-Zr-22	104	201	736	0.52	0.052	0.004	0.235	0.017
ML-Zr-23	71	147	654	0.48	0.056	0.005	0.262	0.023
ML-Zr-24	145	264	680	0.55	0.048	0.003	0.229	0.013
ML-Zr-28	119	211	712	0.56	0.053	0.003	0.248	0.014
ML-Zr-29	144	284	683	0.51	0.056	0.003	0.266	0.013
ML-Zr-30	104	206	691	0.5	0.046	0.003	0.213	0.015
ML-Zr-31	143	377	709	0.38	0.051	0.003	0.229	0.012
ML-Zr-33	154	308	635	0.5	0.056	0.004	0.252	0.019
ML-Zr-35	292	361	666	0.81	0.055	0.002	0.252	0.011
ML-Zr-40	109	211	704	0.52	0.054	0.004	0.251	0.016
ML-Zr-43	108	223	683	0.48	0.055	0.003	0.252	0.015

Analysis	Ratios		Ages (Ma)					
	$^{206}Pb/^{238}U$	2σ	$^{207}Pb/^{206}Pb$	2σ	$^{207}Pb/^{235}U$	2σ	$^{206}Pb/^{238}U$	2σ
ML-Zr-03	0.034	0.000	128	82	207	9	214	3
ML-Zr-04	0.032	0.000	476	161	229	14	205	3
ML-Zr-05	0.033	0.000	392	80	223	9	207	3
ML-Zr-06	0.034	0.000	299	75	222	8	215	2
ML-Zr-09	0.033	0.000	397	67	227	8	211	2
ML-Zr-11	0.034	0.000	214	69	218	8	219	2
ML-Zr-12	0.035	0.000	239	93	222	10	221	3
ML-Zr-13	0.032	0.000	402	187	220	16	203	3
ML-Zr-17	0.034	0.000	125	88	209	9	217	3
ML-Zr-18	0.033	0.001	302	116	219	13	212	3
ML-Zr-19	0.034	0.000	447	134	238	12	218	3
ML-Zr-21	0.033	0.001	326	184	219	15	209	3
ML-Zr-22	0.033	0.001	261	129	214	14	210	4
ML-Zr-23	0.034	0.001	444	206	237	19	216	4
ML-Zr-24	0.034	0.001	119	104	209	11	217	3
ML-Zr-28	0.034	0.001	330	102	225	11	215	3
ML-Zr-29	0.034	0.000	452	82	240	10	218	3
ML-Zr-30	0.033	0.001	9	165	196	13	212	3
ML-Zr-31	0.033	0.000	243	130	209	10	207	2
ML-Zr-33	0.033	0.001	438	181	228	16	208	3
ML-Zr-35	0.033	0.000	422	75	228	9	210	2
ML-Zr-40	0.034	0.001	379	115	227	13	213	3

Table 1 (continued)

Analysis	Ratios		Ages (Ma)					
	$^{206}Pb/^{238}U$	2σ	$^{207}Pb/^{206}Pb$	2σ	$^{207}Pb/^{235}U$	2σ	$^{206}Pb/^{238}U$	2σ
ML-Zr-43	0.033	0.001	421	108	228	12	210	3

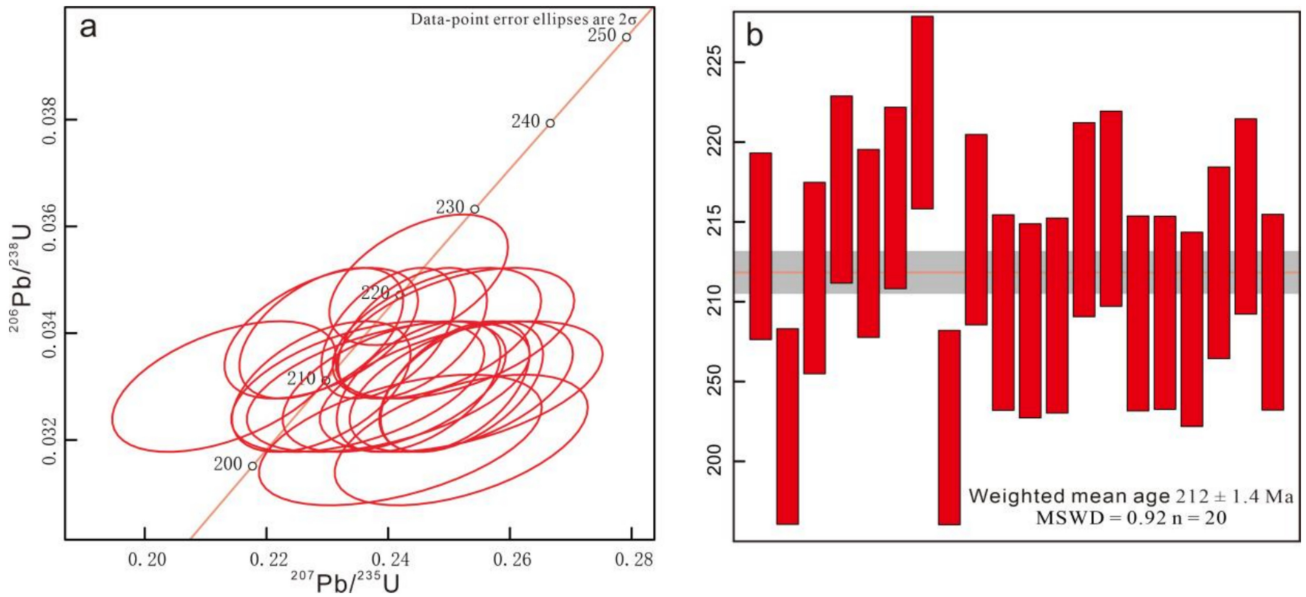

Fig. 4 LA-ICP-MS U–Pb zircon concordia diagrams (**a**) and weighted mean age (**b**) from the Maoerliang diorite

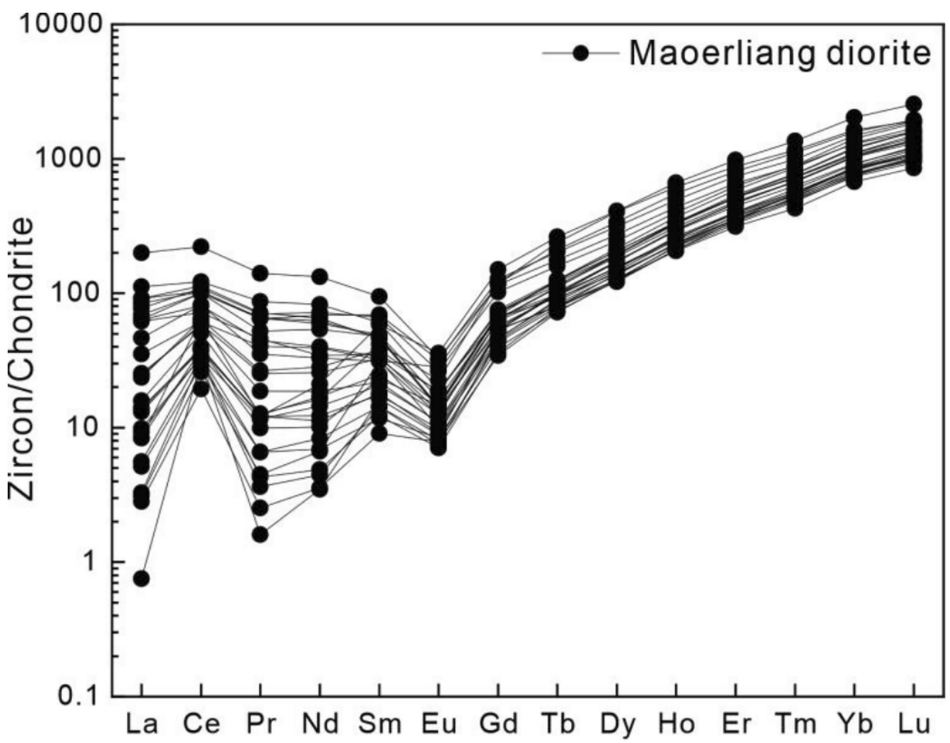

Fig. 5 Chondrite-normalized rare earth element patterns of zircon for the Maoerliang diorite from Sun and McDonough (1989)

Table 2 Trace element composition ($\times 10^{-6}$) of zircons in Maoerliang diorite

Element	La	Ce	Pr	Nd	Sm	Eu	Gd	Tb	Dy
ML-Zr-2	0.18	19.4	0.15	1.62	2.51	0.51	11.3	3.73	43.8
ML-Zr-3	3.12	23.4	1.18	7.95	3.77	0.73	13.1	4.13	49.0
ML-Zr-6	0.67	11.9	0.24	1.67	1.39	0.46	7.06	2.71	31.9
ML-Zr-7	0.03	2.1	0.01	0.15	0.35	0.16	1.84	0.70	8.2
ML-Zr-9	6.02	35.2	1.77	8.70	3.34	0.63	9.55	3.26	37.0
ML-Zr-10	3.75	30.9	1.21	7.60	6.40	1.31	24.5	7.89	85.9
ML-Zr-11	3.35	23.4	1.16	5.73	2.68	0.57	9.20	3.12	34.8
ML-Zr-13	1.33	20.5	0.41	2.28	1.88	0.41	7.40	2.90	32.4
ML-Zr-14	5.60	39.2	2.52	13.2	5.79	1.07	15.0	4.51	49.4
ML-Zr-15	2.19	20.9	0.63	3.23	1.80	0.49	8.09	2.74	31.6
ML-Zr-17	11.0	50.0	3.35	15.36	4.79	0.72	13.2	4.18	47.4
ML-Zr-19	21.6	69.6	6.79	30.4	7.08	0.81	11.0	2.99	31.0
ML-Zr-20	21.7	63.4	6.20	27.9	7.51	0.95	13.7	3.68	39.3
ML-Zr-21	2.34	20.7	1.10	6.76	3.15	0.64	10.9	3.68	43.5
ML-Zr-25	5.80	36.2	2.41	12.0	5.00	0.86	14.6	4.64	52.3
ML-Zr-27	19.89	62.7	6.23	29.0	7.19	0.84	12.9	3.60	39.7
ML-Zr-28	0.74	15.9	0.43	3.11	4.80	1.64	24.4	8.88	102
ML-Zr-30	15.2	61.5	4.95	25.1	7.35	0.82	14.8	4.29	49.5
ML-Zr-31	0.78	19.7	0.35	2.08	2.18	0.43	9.42	3.37	38.3
ML-Zr-32	1.99	39.8	1.15	9.85	8.91	2.07	30.7	9.81	104
ML-Zr-33	47.3	136	13.3	61.8	14.5	1.89	23.7	6.58	69.3
ML-Zr-35	14.6	43.9	4.36	16.1	5.36	1.08	15.4	4.69	52.4
ML-Zr-36	15.1	49.5	4.22	18.7	5.16	0.76	11.7	3.58	39.6
ML-Zr-38	18.3	66.9	6.67	33.6	10.2	1.53	20.9	5.94	62.1
ML-Zr-39	1.99	23.2	0.94	4.72	3.53	0.85	13.9	4.71	54.8
ML-Zr-42	26.5	74.6	8.25	38.5	9.26	1.11	13.6	3.44	36.0
ML-Zr-43	16.4	61.1	6.16	32.1	10.6	1.85	26.3	7.55	79.7
ML-Zr-44	1.22	17.7	0.63	3.89	2.20	0.47	8.87	2.97	35.4
ML-Zr-45	3.22	24.3	1.15	5.23	2.77	0.53	10.8	3.82	43.9

Element	Ho	Er	Tm	Yb	Lu	Y	Ti	ΔFMQ	T (°C)
ML-Zr-2	16.5	73.5	16.0	157	30.4	504	3.90	1.56	813
ML-Zr-3	18.5	85.0	18.5	188	37.9	573	5.33	1.60	847
ML-Zr-6	12.7	58.7	14.0	147	29.5	404	7.56	−0.27	888
ML-Zr-7	3.5	18.4	4.62	50.8	10.0	102	3.63	−1.14	805
ML-Zr-9	14.3	66.5	15.2	155	31.1	447	4.05	2.00	817
ML-Zr-10	31.1	132.9	28.2	269	49.6	890	4.01	2.12	816
ML-Zr-11	13.3	59.0	12.9	130	24.8	396	5.21	1.58	845
ML-Zr-13	12.5	56.5	12.6	125	23.9	378	4.68	1.59	833
ML-Zr-14	18.9	86.3	19.7	203	40.2	592	7.06	1.96	880
ML-Zr-15	11.9	57.5	13.2	138	27.6	391	5.84	1.10	858
ML-Zr-17	17.7	79.8	17.2	175	33.1	525	5.23	2.72	845
ML-Zr-19	11.9	54.6	12.3	127	25.3	364	10.7	2.79	932
ML-Zr-20	14.0	61.3	13.6	132	26.0	413	5.57	3.36	852
ML-Zr-21	16.7	77.2	17.5	177	34.4	499	3.56	2.07	803
ML-Zr-25	19.1	85.6	18.5	182	34.9	585	3.36	2.78	797
ML-Zr-27	14.6	64.3	14.1	142	26.6	442	6.82	3.14	876
ML-Zr-28	34.9	145	29.6	279	48.6	1060	8.56	0.04	904
ML-Zr-30	19.0	88.8	19.7	206	40.2	600	4.34	3.15	824
ML-Zr-31	15.0	66.5	14.5	146	28.2	454	4.92	1.47	838

Table 2 (continued)

Element	Ho	Er	Tm	Yb	Lu	Y	Ti	ΔFMQ	T (°C)
ML-Zr-32	37.6	162	34.6	345	64.7	1097	2.12	2.62	751
ML-Zr-33	24.6	109	22.5	220	40.5	755	7.16	3.96	882
ML-Zr-35	19.1	85.0	18.7	187	36.4	595	5.84	2.53	858
ML-Zr-36	14.5	65.7	14.4	144	27.4	454	4.74	3.02	834
ML-Zr-38	22.5	103.3	22.8	239	46.8	729	2.21	3.87	755
ML-Zr-39	20.9	97.0	21.9	222	42.9	660	5.61	1.51	853
ML-Zr-42	13.1	59.1	12.9	131	25.6	409	8.14	3.58	897
ML-Zr-43	28.0	123	25.3	253	48.2	837	4.40	3.16	826
ML-Zr-44	13.3	62.2	13.8	144	27.4	421	5.89	1.28	859
ML-Zr-45	16.8	77.6	17.2	176	35.2	530	6.08	1.42	862

Zircon Ti-temperature (Ferry and Watson 2007):

$\log(\text{ppm Ti-in-zircon}) = (5.711 \pm 0.072) - (4800 \pm 86) / T(K) - \log aSiO_2 + \log aTiO_2$;

$aSiO_2 = 1$, $aTiO_2 = 0.2$;

Zircon oxygen fugacity (Loucks et al. 2020):

$\Delta FMQ = 3.998(\pm 0.124)\log[Ce/\sqrt{(U_i \times Ti}] + 2.284(\pm 0.101)$

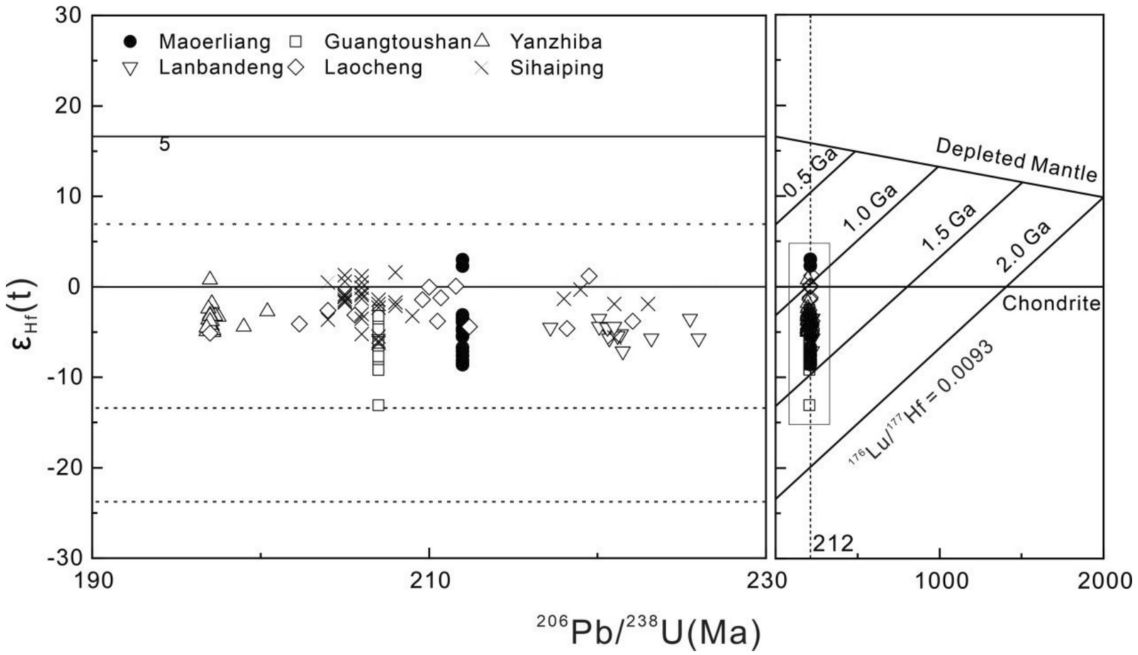

Fig. 6 Zircon $\varepsilon_{Hf}(t)$ value U–Pb age diagram. Date sources: the Guangtoushan pluton (Lu et al. 2016); Yanzhiba, Lanbandeng, and Laocheng pluton (Wang et al. 2021); Sihaiping pluton (Wang et al. 2022)

higher than those of the primitive mantle and continental crust, which may be attributed to the high partition coefficient of Nb over Ta ($D_{Nb}/D_{Ta} > 1$) in the amphibole.

Most zircon grains in the Maoerliang diorite display evolved Lu–Hf isotopic composition, with negative $\varepsilon_{Hf}(t)$ values of −8.6 to +3.0, with corresponding two-stage model age of 886 to 1479 Ma, indicating a crust–mantle mixed source. The minor grains which display positive $\varepsilon_{Hf}(t)$ values indicate the incorporation of depleted mantle components, which is similar to the Laocheng, Yanzhiba, and Sihaiping diorite in the Triassic Ningshan pluton (Fig. 5) (Wang et al. 2021). According to the evolved Nd isotopic compositions, $\varepsilon_{Nd}(t) = -3.7$ to 2.5, with corresponding two-stage model ages of 1.17 to 1.44 Ga) of the Triassic granites in the Qinling orogenic belt, Zhang et al (1997) proposed that these Triassic granites mainly derived from dehydration melting of the Neoproterozoic crystalline basement, e.g., the Neoproterozoic Yaolinghe meta-basalts (Zhang et al. 1997). The

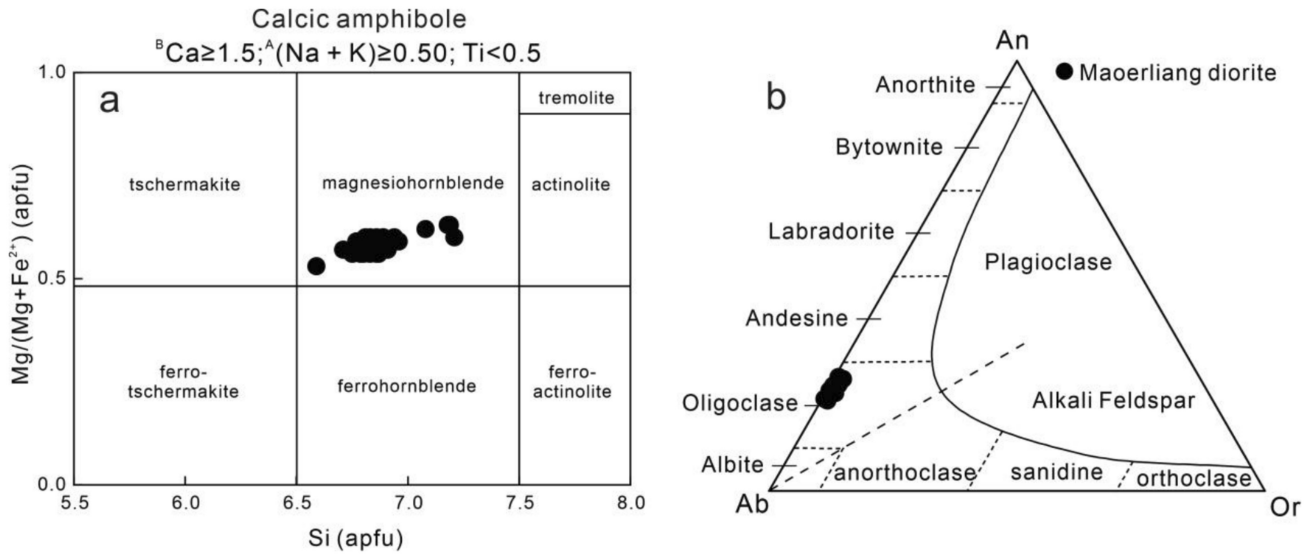

Fig. 7 Mineral composition in the Maoerliang diorite. **a** Composition of amphibole (after Leake et al. 1997); **b** An-Ab-Or diagram of plagioclase

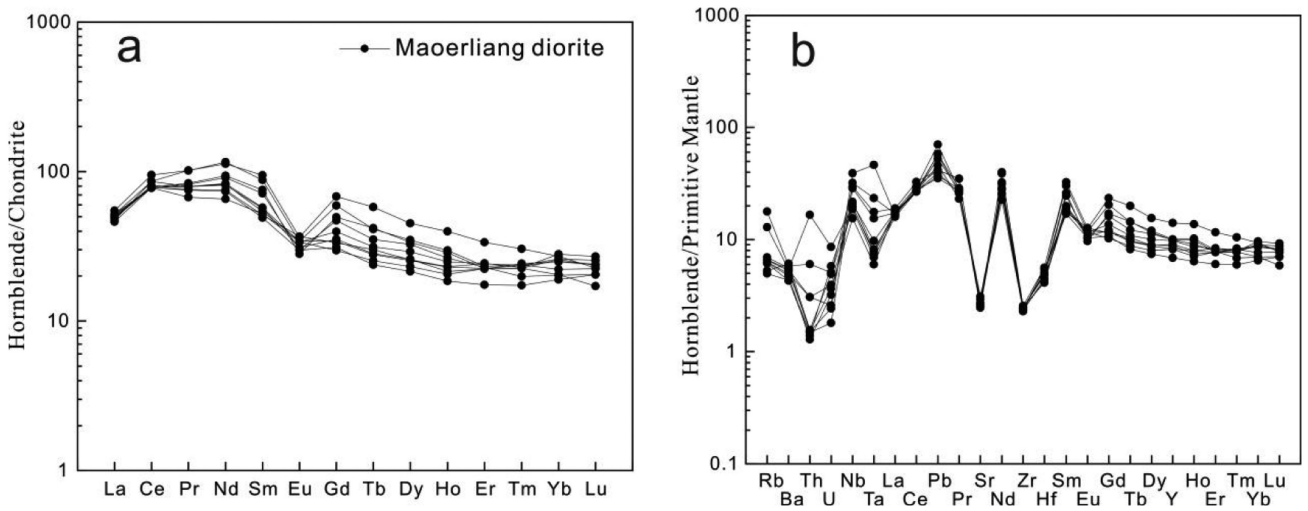

Fig. 8 Chondrite-normalized rare earth element patterns (**a**) and primitive mantle-normalized spider diagram (**b**) of amphiboles for the Maoerliang diorite from Sun and McDonough (1989)

Maoerliang diorites share similar isotopic composition with these Triassic granites, indicating a common source region.

5.2 Crystallization conditions and oxygen fugacity

Amphibole has the chemical formula $A_{0\text{-}1}B_2C_5[T_8O_{22}](OH)_2$, which can preserve information about crystallization temperature, pressure, H_2O content, and oxygen fugacity of the primitive dioritic magma. Ridolfi et al. (2010) proposed a refined calculation model to calculate the crystallization temperature, pressure, H_2O content, and oxygen fugacity in igneous rocks, based on a comparison between natural amphibole compositions in calc-alkaline igneous rocks and experimental works. Through extensive verification of natural amphibole compositions, Erdmann et al. (2014) concluded that the model proposed by Ridolfi et al. (2010) is reasonable. Therefore, we use the Ridolfi et al. (2010) model to calculate the crystallization condition of

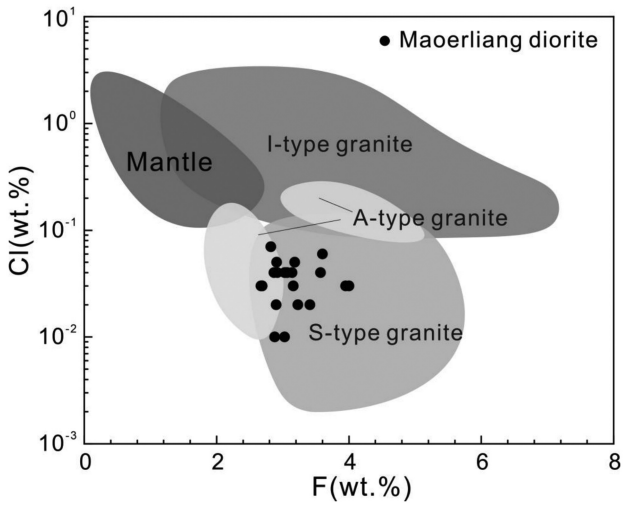

Fig. 9 Diagrams of F content versus Cl of apatites for the Maoerliang diorite (modified from Zhou et al. 2022)

the Maoerliang diorite. The results indicate that amphibole in the diorite has crystallization temperatures ranging from 805 to 866 ± 57 °C, with an average of 853 °C, and pressures ranging from 211 to 383 ± 60 MPa, with an average of 368 MPa. According to the crustal average density of 2700 kg/m^3, the corresponding emplacement depth is 8.0–14.5 km, with an average of 12.4 km, indicating a deep-level crystallization condition.

The H_2O content and oxygen fugacity are calculated according to the chemical features of the amphibole using the methods of Ridolfi et al. (2010). The results indicate that the Maoerliang diorite has high H_2O content of 4.22–4.94% and oxygen fugacity (ΔNNO = −4.08 to −3.71, logf_{O2} = −12.0 to −13.7). The high H_2O content in silicate melt would promote crystallization of amphibole and delay crystallization of plagioclase (Nekvasil et al. 2004), which is confirmed by the clinopyroxene inclusions in amphibole (Fig. 2) and low An values of the plagioclase (An = 21–26). The apatites that crystallized from mantle-derived magma would have low F/Cl ratios (Fig. 9; Zhou et al. 2022). The apatites in the diorite have high F and low Cl content, with high F/Cl ratios of 77 to 690. The low Cl content of these apatites indicates that they may have crystallized in magma derived from hydrated crust, indicating the existence of evolved crustal components in their source (Zafar et al. 2020). In addition, most of the points in the F vs. Cl diagram fall into the S-type granite area (Fig. 9), which is consistent with the conclusion of previous studies in the Triassic Ningshan pluton (Wang et al. 2021).

Zircon is ubiquitous in various types of rocks, serving as an important accessory mineral. Its stable physical and chemical properties record a range of information including magmatic crystallization age, temperature, and oxygen fugacity, making it widely used in solid Earth geochemical research (Ballard et al. 2002; Ferry and Watson 2007; Zou et al. 2019; Loucks et al. 2020; Niu et al. 2024). When applying trace elements in zircon to calculate temperature and oxygen fugacity, different calculation methods have varying principles and application conditions, which may lead to deviations in the calculated results. Therefore, selection of the appropriate calculation method is essential. The zircon Ti thermometer uses the method of Ferry and Watson (2007). To obtain useful temperatures, it is necessary to make reasonable estimates of the activity of TiO_2 and SiO_2. The diorite contains quartz, magnetite, and ilmenite, so the activity of SiO_2 is buffered at 1, and the activity of TiO_2 is buffered at 0.2. The calculated zircon Ti-temperatures range from 751 to 932 °C, with an average of 843 °C, which is consistent with the crystallization temperature of amphibole. In the Maoerliang diorites, the overall high La content in zircon ranging from 0.18 to 47.3 ppm suggests a higher content of inclusions (e.g., apatite) within the zircon. Loucks et al. (2020) utilized the correlation between Ce, U, and Ti in zircon to propose a Ce–U–Ti oxygen fugacity meter for zircon, which can effectively avoid the influence of zircon crystallization temperature and mineral inclusions. The calculated results show that ΔFMQ ranges from −1.14 to +3.96, with an average of +2.07, and logf_{O2} ranges from −13.3 to −19.9, slightly higher than mantle wedge oxygen fugacity (ΔFMQ = −1 to +2).

Early studies on the East Qinling gold deposits suggested that magma activity characterized by high oxygen fugacity and high H_2O content, which are rich in mantle materials, is favorable for the formation of gold deposits (Zhi et al. 2019; Li et al. 2022; Liu et al. 2022; Wen et al. 2023; Wei et al. 2024). We compared the zircon oxygen fugacity and zircon Ti-temperature of the Maoerliang diorite, the Mo-W-bearing granite in the Ningshan area, and the Au-bearing granite in the East Qinling (Fig. 11; Wen et al. 2023). The results show that the oxygen fugacity of the Maoerliang barren diorite is higher than that of the W-Mo-bearing granite from the same source region, but it is similar to that of the Au-bearing granite in the East Qinling. The deep mantle/crust is an important source of ore-forming materials, and fluids rich in F and with high oxygen fugacity are conducive to the precipitation of Au and other ore-forming elements. Since the Maoerliang diorite has characteristics similar to gold-bearing granite, the study of the Maoerliang diorite has certain reference value for gold exploration in the South Qinling.

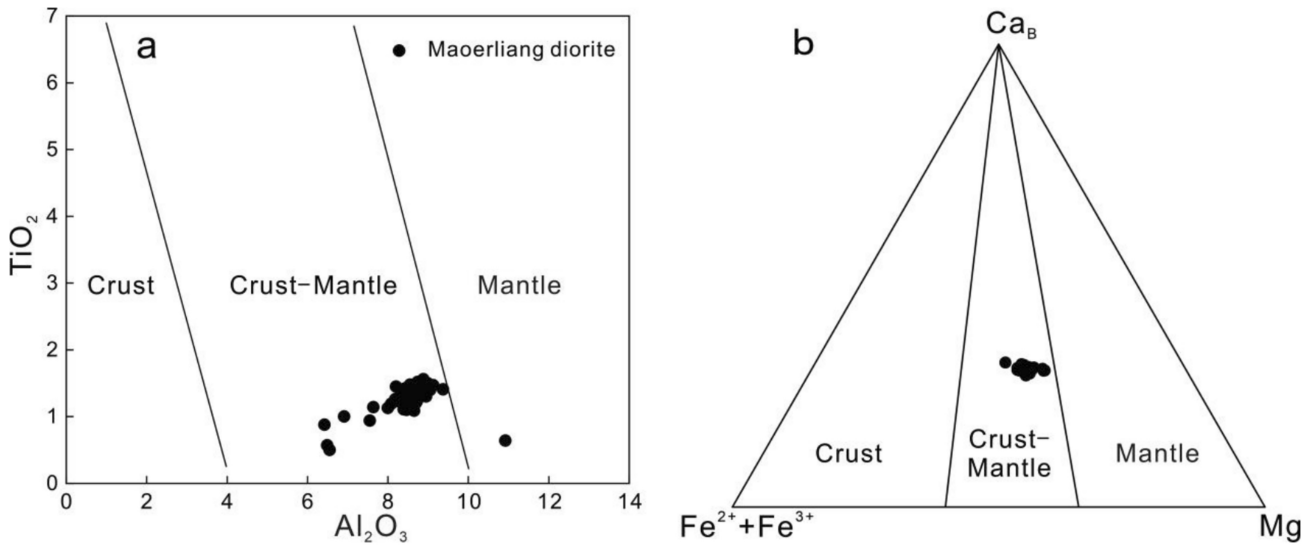

Fig. 10 Origin diagram of amphibole for the Maoerliang diorite. **a** TiO_2 versus Al_2O_3 diagram (after Jiang and An 1984) and **b** Ca_B-($Fe^{2+}+Fe.^{3+}$)-Mg diagram (Xie and Zhang 1990)

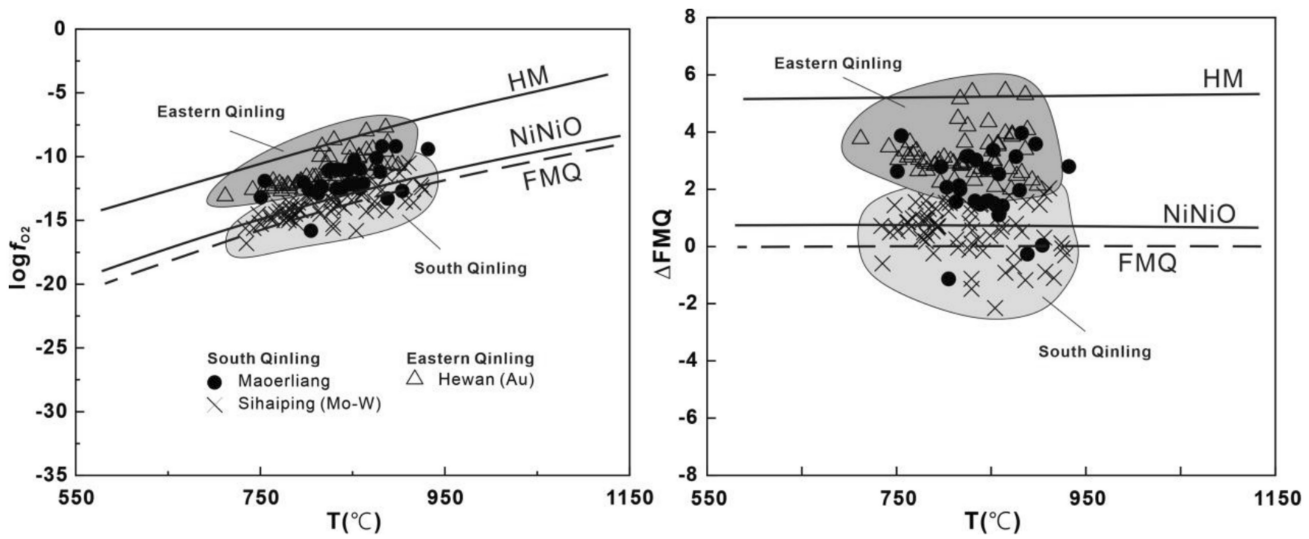

Fig. 11 **a** Logf_{O2} vs. T diagrams and **b** ΔFMQ vs. T of zircon for the Maoerliang diorite (data for the Sihaiping giant Mo-W deposits were calculated based on Wang et al. data for the Hewan giant Au deposits were calculated based on Wen et al. 2023)

6 Conclusions

1. The Maoerliang diorite exhibits a zircon U–Pb age of 212 ± 2.8 Ma, which coincides with the Late-Triassic granitic magmatism in the Qinling Orogenic Belt. The evolved zircon Hf isotopic compositions, $\varepsilon_{Hf}(t) = -8.6$ to +3.0, and amphibole composition indicate that the primitive dioritic magma was derived from a crust–mantle mixing source.
2. Based on the temperature–pressure date from amphibole and zircon, the dioritic magma crystallization temperature ranged from 805 to 866 °C and pressure ranged from 211 to 383 MPa. This high oxygen fugacity (ΔNNO = −4.08 to −3.71; ΔFMQ = −1.14 to +3.96) and relatively high H_2O content (4.22%–4.94%) indicate hydrous melting underplating beneath the lower crust. This process has significant implications for granite genesis and crustal evolution, and will aid the prospecting work of the South Qinling gold deposit.

Acknowledgements This work was supported by the National Natural Science Foundation of China (42372071, 41102037), Shaanxi

public welfare geological survey project (202409), and the Foundation for the Author of National Excellent Doctoral Dissertation of China (201324).

Author contributions Jiangfeng Qin conceived the study and performed the fieldwork; Hua Zhang conducted the laboratory analyses and contributed to the interpretation of the data, and drafted the manuscript; Jiangfeng Qin examined and revised the manuscript; Kai Zhang, Xi Zhu, Shaohua Mao, and Lisha Bi provided critical feedback and helped shape the research, analysis, and manuscript. All authors contributed to the final version of the manuscript.

Declarations

Conflict of interest The authors declare that they have no conflict of interest.

Ethical approval No conflict of interest exits in the submission of this manuscript, and the manuscript is approved by all authors for publication. I would like to declare on behalf of my co-authors that the work described was original research that has not been published previously, and not under consideration for publication elsewhere, in whole or in part. All the authors listed have approved the manuscript.

References

Anderson JL, Smith DR (1995) The effects of temperature and f_{O2} on the Al-in-hornblende barometer. Am Mineral 80(5–6):549–559. https://doi.org/10.2138/am-1995-5-614

Ballard JR, Palin JM, Campbell IH (2002) Relative oxidation states of magmas inferred from Ce(IV)/Ce(III) in zircon: Application to porphyry copper deposits of northern Chile. Contrib Mineral Petrol 144(3):347–364. https://doi.org/10.1007/s00410-002-0402-5

Bao ZA, Yuan HL, Zong CL, Liu Y, Chen KY, Zhang YL (2016) Simultaneous determination of trace elements and lead isotopes in fused silicate rock powders using a boron nitride vessel and fsLA-(MC)-ICP-MS. J Anal at Spectrom 31(4):1012–1022. https://doi.org/10.1039/C5JA00410A

Castro A, Corretgé LG, de la Rosa JD, Fernández C, López S, García-Moreno O, Chacón H (2003) The appinite–migmatite complex of sanabria, NW Iberian massif. Spain J Petrol 44(7):1309–1344

Chang J, Audétat A, Li J-W (2021) In situ reaction-replacement origin of hornblendites in the early cretaceous laiyuan complex, North China Craton, and implications for its Tectono-magmatic evolution. J Petrol 62. https://doi.org/10.1093/petrology/egab030

Chen YJ, Pirajno F, Li N, Guo DS, Lai Y (2009) Isotope systematics and fluid inclusion studies of the Qiyugou breccia pipe-hosted gold deposit, Qinling Orogen, Henan province, China: Implications for ore genesis. Ore Geol Rev 35(2):245–261. https://doi.org/10.1016/j.oregeorev.2008.11.003

Collins WJ, Murphy JB, Johnson TE, Huang HQ (2020) Critical role of water in the formation of continental crust. Nat Geosci 13:331–338. https://doi.org/10.1038/s41561-020-0573-6

Deng ZB, Liu SW, Zhang WY, Hu FY, Li QG (2016) Petrogenesis of the Guangtoushan granitoid suite, Central China: Implications for Early Mesozoic geodynamic evolution of the Qinling Orogenic Belt. Gondwana Res 30:112–131. https://doi.org/10.1016/j.gr.2015.07.012

Dong YP, Santosh M (2016) Tectonic architecture and multiple orogeny of the Qinling Orogenic Belt. Central China Gondwana Res 29(1):1–40. https://doi.org/10.1016/j.gr.2015.06.009

Dong YP, Zhang GW, Neubauer F, Liu XM, Genser J, Hauzenberger C (2011) Tectonic evolution of the Qinling Orogen, China: Review and synthesis. J Asian Earth Sci 41(3):213–237. https://doi.org/10.1016/j.jseaes.2011.03.002

Dong YP, Liu XM, Santosh M, Chen Q, Zhang XN, Li W, He DF, Zhang GW (2012) Neoproterozoic accretionary tectonics along the northwestern margin of the Yangtze Block, China: Constraints from zircon U-Pb geochronology and geochemistry. Precambrian Res 196:247–274. https://doi.org/10.1016/j.precamres.2011.12.007

Dong YP, Liu XM, Neubauer F, Zhang GW, Tao N, Zhang YG, Zhang XN, Li W (2013) Timing of Paleozoic amalgamation between the North China and South China blocks: Evidence from detrital zircon U-Pb ages. Tectonophysics 586:173–191. https://doi.org/10.1016/j.tecto.2012.11.018

Dong YP, Yang Z, Liu XM, Zhang XN, He DF, Li W, Zhang FF, Sun SS, Zhang HF, Zhang GW (2014) Neoproterozoic amalgamation of the northern Qinling terrain to the North China Craton: Constraints from geochronology and geochemistry of the Kuanping ophiolite. Precambrian Res 255:77–95. https://doi.org/10.1016/j.precamres.2014.09.008

Dong YP, Sun SS, Santosh M, Zhao J, Sun JP, He DF, Shi XH, Hui B, Cheng C, Zhang GW (2021) Central China Orogenic Belt and amalgamation of east Asian continents. Gondwana Res 100:131–194. https://doi.org/10.1016/j.gr.2021.03.006

Erdmann S, Martel C, Pichavant M, Kushnir A (2014) Amphibole as an archivist of magmatic crystallization conditions: Problems, potential, and implications for inferring magma storage prior to the paroxysmal 2010 eruption of Mount Merapi. Indonesia Contrib Mineral Petrol 167(6):1016. https://doi.org/10.1007/s00410-014-1016-4

Ferry JM, Watson EB (2007) New thermodynamic models and revised calibrations for the Ti-in-zircon and Zr-in-rutile thermometers. Contrib Mineral Petrol 154(4):429–437. https://doi.org/10.1007/s00410-007-0201-0

He J, Fan X, Zhao JX, Huo DY, Zhang NZ, Chen FK (2023) Petrogenesis of the Triassic Dongjiangkou pluton in the South Qinling orogenic belt, Central China: Insufficient magma mixing of mafic and felsic magmas. Lithos 456:107312. https://doi.org/10.1016/j.lithos.2023.107312

Hu FY, Liu SW, Santosh M, Deng ZB, Wang W, Zhang WY, Yan M (2016) Chronology and tectonic implications of Neoproterozoic blocks in the south Qinling Orogenic Belt, Central China. Gondwana Res 30:24–47. https://doi.org/10.1016/j.gr.2015.01.006

Iveson AA, Humphreys MCS, Savov IP, de Hoog JCM, Turner SJ, Churikova TG, Macpherson CG, Mather TA, Gordeychik BN, Tomanikova L, Agostini S, Hammond K, Pyle DM, Cooper GF (2021) Deciphering variable mantle sources and hydrous inputs to arc magmas in Kamchatka. Earth Planet Sci Lett 562:116848. https://doi.org/10.1016/j.epsl.2021.116848

Jiang CY, An SY (1984) On chemical characteristics of calcic amphiboles from igneous rocks and their petrogenesis significance. Mineral Petrol 3:1–9. https://doi.org/10.19719/j.cnki.1001-6872.1984.03.001

Laurent O, Zeh A, Gerdes A, Villaros A, Gros K, Słaby E (2017) How do granitoid magmas mix with each other? Insights from textures, trace element and Sr–Nd isotopic composition of apatite and titanite from the Matok pluton (South Africa). Contr Mineral Petrol 172(9):80. https://doi.org/10.1007/s00410-017-1398-1

Leake BE, Woolley AR, Arps CES, Birch WD, Gilbert MC, Grice JD, Hawthorne E, Kato A, Kisch HJ, Krivovichev VG, Linthout K, Laird J, Mandarino J, Maresch WV, Nickel EH, Rock NMS, Schumacher JC, Smith DC, Stephenson NCN, Ungaretti L, Whittaker EJW, Youzhi G (1997) Nomenclature of amphiboles report of the subcommittee on amphiboles of the international mineralogical association commission on new minerals and mineral names. Ejm 9(3):623–651. https://doi.org/10.1127/ejm/9/3/0623

Leite AFGD, Fuck RA, Dantas EL, Ruiz AS (2021) Appinitic and high BaSr magmatism in central Brazil: Insights into the late accretion stage of West Gondwana. Lithos 398–399:106333. https://doi.org/10.1016/j.lithos.2021.106333

Li L, Li C, Li Q, Yuan MW, Zhang JQ, Li SR, Santosh M, Shen JF, Zhang HF (2022) Indicators of decratonic gold mineralization in the North China Craton. Earth Sci Rev 228:103995. https://doi.org/10.1016/j.earscirev.2022.103995

Liu YS, Hu ZC, Gao S, Günther D, Xu J, Gao CG, Chen HH (2008) *In situ* analysis of major and trace elements of anhydrous minerals by LA-ICP-MS without applying an internal standard. Chem Geol 257(1–2):34–43. https://doi.org/10.1016/j.chemgeo.2008.08.004

Liu SW, Li QG, Tian W, Wang ZQ, Yang PT, Wang W, Bai X, Guo RR (2011) Petrogenesis of Indosinian granitoids in middle-segment of south Qinling tectonic belt: Constraints from Sr-Nd isotopic systematics. Acta Geologica Sinica (Eng) 85(3):610–628. https://doi.org/10.1111/j.1755-6724.2011.00455.x

Liu JW, Li L, Li SR, Santosh M, Yuan MW (2022) Apatite as a fingerprint of granite fertility and gold mineralization: Evidence from the Xiaoqinling Goldfield. North China Craton Ore Geol Rev 142:104720. https://doi.org/10.1016/j.oregeorev.2022.104720

Loucks RR, Fiorentini ML, Henríquez GJ (2020) New magmatic oxybarometer using trace elements in zircon. J Petrol 61(3):egaa034. https://doi.org/10.1093/petrology/egaa034

Lu YH, Zhao ZF, Zheng YF (2016) Geochemical constraints on the source nature and melting conditions of Triassic granites from South Qinling in Central China. Lithos 264:141–157. https://doi.org/10.1016/j.lithos.2016.08.018

Ludwig KR (2003) ISOPLOT 3.0: A geochronological toolkit for microsoft excel, Berkeley Geochronology Center Spe publ No. 4.

Murphy JB (2013) Appinite suites: A record of the role of water in the genesis, transport, emplacement and crystallization of magma. Earth Sci Rev 119:35–59. https://doi.org/10.1016/j.earscirev.2013.02.002

Murphy JB (2020) Appinite suites and their genetic relationship with coeval voluminous granitoid batholiths. Int Geol Rev 62(6):683–713. https://doi.org/10.1080/00206814.2019.1630859

Nekvasil H, Dondolini A, Horn J, Filiberto J, Long H, Lindsley DH (2004) The origin and evolution of silica-saturated alkalic suites: An experimental study. J Petrol 45(4):693–721

Niu JL, Wu ST, Yang YH, Zhang C, Wang H, Gong QJ (2024) Application of 'Ti-in-quartz and Ti-in-zirconthermometers in geoscience and progress of microbeam analysis technology of Ti content. Acta Petrologica Sinica 40(1):323–337. https://doi.org/10.18654/1000-0569/2024.01.18

Pe-Piper G, Piper DJW (2018) The Jeffers Brook diorite–granodiorite pluton: Style of emplacement and role of volatiles at various crustal levels in Avalonian appinites. Canadian Appalachians Int J Earth Sci 107(3):863–883. https://doi.org/10.1007/s00531-017-1536-z

Qin KL, Song SG, He SP (1992) The geological characteristics of the Yudongzi granite-greenstone terrain and its gold-bearing property in mianluening area Shaanxi. Northwest Geosci 1:65–74

Qin JF, Lai SC, Wang J, Li YF (2007) High-Mg# adakitic tonalite from the xichahe area, south Qinling Orogenic Belt (Central China): Petrogenesis and geological implications. Int Geol Rev 49(12):1145–1158. https://doi.org/10.2747/0020-6814.49.12.1145

Qin JF, Lai SC, Diwu CR, Ju YJ, Li YF (2010) Magma mixing origin for the post-collisional adakitic monzogranite of the Triassic Yangba pluton, Northwestern margin of the South China block: Geochemistry, Sr–Nd isotopic, zircon U-Pb dating and Hf isotopic evidences. Contrib Mineral Petrol 159(3):389–409. https://doi.org/10.1007/s00410-009-0433-2

Qin JF, Lai SC, Li YF (2013) Multi-stage granitic magmatism during exhumation of subducted continental lithosphere: Evidence from the Wulong pluton. South Qinling Gondwana Res 24(3–4):1108–1126. https://doi.org/10.1016/j.gr.2013.02.005

Qin JF, Lai SC, Long XP, Li YF, Ju YJ, Zhao SW, Zhu RZ, Wang JB, Zhang ZZ (2019) Hydrous melting of metasomatized mantle wedge and crustal growth in the post-collisional stage: Evidence from Late Triassic monzodiorite and its mafic enclaves in the south Qinling (Central China). Lithosphere 11(1):3–20. https://doi.org/10.1130/l1006.1

Ridolfi F, Renzulli A, Puerini M (2010) Stability and chemical equilibrium of amphibole in calc-alkaline magmas: An overview, new thermobarometric formulations and application to subduction-related volcanoes. Contrib Mineral Petrol 160(1):45–66. https://doi.org/10.1007/s00410-009-0465-7

Shi Y, Yu JH, Santosh M (2013) Tectonic evolution of the Qinling Orogenic Belt, Central China: New evidence from geochemical, zircon U-Pb geochronology and Hf isotopes. Precambrian Res 231:19–60. https://doi.org/10.1016/j.precamres.2013.03.001

Stern RA, Hanson GN, Shirey SB (1989) Petrogenesis of mantle-derived, LILE-enriched Archean monzodiorites and trachyandesites (sanukitoids) in southwestern Superior Province. Can J Earth Sci 26(9):1688–1712. https://doi.org/10.1139/e89-145

Sun SS, McDonough WF (1989) Chemical and isotopic systematics of oceanic basalts: Implications for mantle composition and processes. Geol Soc Lond Spec Publ 42(1):313–345. https://doi.org/10.1144/gsl.sp.1989.042.01.19

Tarney J, Jones CE (1994) Trace element geochemistry of orogenic igneous rocks and crustal growth models. J Geol Soc 151(5):855–868. https://doi.org/10.1144/gsjgs.151.5.0855

Wang XX, Wang T, Castro A, Pedreira R, Lu XX, Xiao QH (2011a) Triassic granitoids of the Qinling Orogen, Central China: Genetic relationship of enclaves and rapakivi-textured rocks. Lithos 126(3–4):369–387. https://doi.org/10.1016/j.lithos.2011.07.007

Wang XX, Wang T, Qi QJ, Li S (2011b) Temporal-spatial variations, origin and their tectonic significance of the Late Mesozoic granites in the Qinling. Central China Acta Petrol Sin 27(6):1573–1593

Wang XX, Wang T, Zhang CL (2015) Granitoid magmatism in the Qinling orogen, central China and its bearing on orogenic evolution. Scientia Sinica Terrae 45(08):1109–1125. https://doi.org/10.1007/s11430-015-5150-2

Wang RX, Li XW, Guan Q, Sun YQ, Li RZ, Xie PL, Wu BB, Xia WY (2021) Source compositions and peritectic assemblage entrainment as the main compositional driver in the granitoids: A case study of the Ningshan granitic plutons in South Qinling. Acta Petrologica Sinca 37(12):3815–3848. https://doi.org/10.18654/1000-0569/2021.12.13

Wei Q, Li L, Li SR, Santosh M, Alam M, Chen ZY, Li MG, Chen XD, Wen ZH, Liu JW (2024) Titanite as an indicator of granite fertility and gold mineralization in the Xiaoqinling gold province. North China Craton Front Earth Sci 12:1487176. https://doi.org/10.3389/feart.2024.1487176

Wen ZH, Li L, Harlov DE, Li SR (2023) Zircon constraints on gold enrichment in a high-silica porphyry, Yixingzhai region, north of the Trans-North China Orogen. Lithos 444–445:107099. https://doi.org/10.1016/j.lithos.2023.107099

Wiedenbeck M, Allé P, Corfu F, Griffin WL, Meier M, Oberli F, Von Quadt A, Roddick JC, Spiegel W (1995) Three natural zircon standards for U-Th-Pb, lu-hf, trace element and REE analyses. Geostand Newsl 19(1):1–23. https://doi.org/10.1111/j.1751-908x.1995.tb00147.x

Wu FY, Li XH, Zheng YF, Gao S (2007) Lu-Hf isotopic systematics and their applications in petrology. Acta Petrologica Sinca 02:185–220. https://doi.org/10.3969/j.issn.1000-0569.2007.02.001

Wu YB, Zhou GY, Gao S, Liu XC, Qin ZW, Wang H, Yang JZ, Yang SH (2014) Petrogenesis of Neoarchean TTG rocks in the Yangtze Craton and its implication for the formation of Archean TTGs.

Precambrian Res 254:73–86. https://doi.org/10.1016/j.precamres.2014.08.004

Xie YW, Zhang YQ (1990) Peculiarities and genetic significance of hornblende from granite in the Hengduansan region. Acta Mineralogica Sinca 10(1):35–45. https://doi.org/10.16461/j.cnki.1000-4734.1990.01.006

Yang PT, Liu SW, Li QG, Zhang F, Wang ZQ, Wang DS, Wang RT, Yan QR, Yan Z (2011) Ages of the Laocheng granitoids and crustal growth in the south Qinling tectonic domain, Central China: Zircon U-Pb and Lu-Hf isotopic constraints. Acta Geologica Sinica (Eng) 85(4):854–869. https://doi.org/10.1111/j.1755-6724.2011.00490.x

Yang PT, Liu SW, Li QG, Wang ZQ, Zhang F, Wang W (2013) Chronology and petrogenesis of the Hejiazhuang granitoid pluton and its constraints on the Early Triassic tectonic evolution of the South Qinling Belt. Sci Sin Terrae 43(11):1874–1893

Yang PT, Liu SW, Li QG, Wang ZQ, Zhang F, Wang W (2014) Chronology and petrogenesis of the Hejiazhuang granitoid pluton and its constraints on the Early Triassic tectonic evolution of the South Qinling Belt. Sci China Earth Sci 57(2):232–246. https://doi.org/10.1007/s11430-013-4666-6

Yuan HL, Gao S, Dai MN, Zong CL, Günther D, Fontaine GH, Liu XM, Diwu CR (2008) Simultaneous determinations of U-Pb age, Hf isotopes and trace element compositions of zircon by excimer laser-ablation quadrupole and multiple-collector ICP-MS. Chem Geol 247(1–2):100–118. https://doi.org/10.1016/j.chemgeo.2007.10.003

Yuan LL, Zhang XH, Zhai MG, Xue FH (2016) Petrogenesis and geodynamic implications of appinite suite. Acta Petrol Sin 32(5):1556–1570

Zafar T, Rehman HU, Ali Mahar M, Alam M, Oyebamiji A, Rehman SU, Leng CB (2020) A critical review on petrogenetic, metallogenic and geodynamic implications of granitic rocks exposed in north and East China: New insights from apatite geochemistry. J Geodyn 136:101723. https://doi.org/10.1016/j.jog.2020.101723

Zhang GF, Zhang BR, Lin WL, Gao S, Ouyang JP (1997) Neoproterozoic crustal accretion event in southern Qinling: Nd isotope tracing of granitic rocks. Geochimica 05:16–24

Zhang GW, Zhang BR, Yuan XC, Xiao QH (2001) Qinling orogenic belt and continental dynamics. Science Press, Beijing (in Chinese with English abstract)

Zhang CL, Wang T, Wang XX (2008) Origin and tectonic setting of the Early Mesozoic granitoids in Qinling Orogenic Belt. Geological J China Uni 03:304–316. https://doi.org/10.3969/j.issn.1006-7493.2008.03.003

Zhang X, Xu XY, Song GS, Wang HL, Cheng JL, Li T (2010) Zircon LA-ICP-MS U-Pb dating and significance of Yudongzi Group deformation granite from Lueyang area, western Qinling, China. Geological Bulletin of China. Geol Bull China 29(04):510–517. https://doi.org/10.3969/j.issn.1671-2552.2010.04.004

Zhang X, Xue F, Yuan L, Ma Y, Wilde SA (2012) Late Permian appinite–granite complex from northwestern Liaoning, North China Craton: Petrogenesis and tectonic implications. Lithos 155:201–217. https://doi.org/10.1016/j.lithos.2012.09.002

Zhang H, Wu GH, Cheng H, Ye RS, He JF, Chen FK (2019) Late Triassic high Mg diorites of the Wulong pluton in the South Qinling Belt, China: Petrogenesis and implications for crust-mantle interaction. Lithos 332:135–146. https://doi.org/10.1016/j.lithos.2019.01.038

Zhi ZY, Li L, Li SR, Santosh M, Yuan MW, Alam M (2019) Magnetite as an indicator of granite fertility and gold mineralization: A case study from the Xiaoqinling gold province. North China Craton Ore Geol Rev 115:103159. https://doi.org/10.1016/j.oregeorev.2019.103159

Zhong YF, Wang LX, Zhao JH, Liu L, Ma CQ, Zheng JP, Zhang ZJ, Luo BJ (2016) Partial melting of an ancient sub-continental lithospheric mantle in the Early Paleozoic intracontinental regime and its contribution to petrogenesis of the coeval peraluminous granites in South China. Lithos 264:224–238. https://doi.org/10.1016/j.lithos.2016.08.026

Zhou BQ, Sun JF, Yang JH (2022) *In-situ* apatite geochemical and isotopic insights into the petrogenesis of granitoids. Acta Petrologica Sinca 38(12):3853–3867. https://doi.org/10.18654/1000-0569/2022.12.20

Zou XY, Qin KZ, Han XL, Li GM, Evans NJ, Li ZZ, Yang W (2019) Insight into zircon REE oxy-barometers: A lattice strain model perspective. Earth Planet Sci Lett 506:87–96. https://doi.org/10.1016/j.epsl.2018.10.031

Publisher's Note Springer Nature remains neutral with regard to jurisdictional claims in published maps and institutional affiliations.

Springer Nature or its licensor (e.g. a society or other partner) holds exclusive rights to this article under a publishing agreement with the author(s) or other rightsholder(s); author self-archiving of the accepted manuscript version of this article is solely governed by the terms of such publishing agreement and applicable law.